Structural and dynamical properties for confined polymers undergoing planar Poiseuille flow

Junfang Zhang,[a] J. S. Hansen, and B. D. Todd[b]
Center for Molecular Simulation, Swinburne University of Technology, P.O. Box 218, Hawthorn, Victoria 3122, Australia

Peter J. Daivis
Applied Physics, School of Applied Sciences, RMIT University, GPO Box 2476V, Melbourne, Victoria 3001, Australia

(Received 16 November 2006; accepted 13 February 2007; published online 11 April 2007)

The authors present the results from nonequilibrium molecular dynamics simulations for the structural and dynamical properties of highly confined linear polymer fluids undergoing planar Poiseuille flow. They study systems confined within pores of several atomic diameters in width and investigate the dependence of the density profiles, the mean squared radius of gyration, the mean squared end-to-end distance, streaming velocity, strain rate, shear stress, and streaming angular velocity as functions of average fluid density and chain length. Their simulation results show that, sufficiently far from the walls, the radius of gyration for molecules under shear in the middle of the pore follows the power law $R_g = AN_b^{\nu}$, where N_b is the number of bonds and the exponent has a value of 0.5 which resembles the value for a homogeneous equilibrium fluid. Under the conditions simulated, the authors find the onset of flat velocity profiles but with very little wall slippage. These flat profiles are most likely due to the restricted layering of the fluid into just one or two molecular layers for narrow pore widths compared to chain length, rather than typical plug-flow conditions. The angular velocity is shown to be proportional to half the strain rate in the pore interior when the chain length is sufficiently small compared to the pore width, consistent with the behavior for homogeneous fluids in the linear regime. © *2007 American Institute of Physics*.
[DOI: 10.1063/1.2714556]

I. INTRODUCTION

The properties of confined fluids can differ markedly from those of the corresponding bulk fluid. These differences arise from the competition between the interatomic forces operating between fluid atoms and the interatomic forces acting on fluid and confining wall atoms. The study of the rheology of polymeric fluids in nanoporous materials is very important because of their potential usefulness in technological applications as well as their intrinsic scientific interest. When a fluid is narrowly confined within spacing comparable to molecular dimensions, its structural and dynamic properties deviate strongly from the bulk behavior in various respects. It was previously shown that a deviation from typical quadratic velocity profiles predicted by classical Navier-Stokes theory can be observed for planar Poiseuille flow.[1] The shear stress exhibits oscillations about the classical linear profile, and highly layer-structured density profiles are present. Strong density variations across the fluid pore result in spatial inhomogeneities in all transport properties[2–4] that deviate substantially from their bulk properties.

An understanding of these properties can be very important in many applications such as materials synthesis. In fact, these properties of confined fluids are far from fully understood, primarily due to the failure of continuum theories at such small length scales and the apparent difficulty of current experimental techniques in probing the transport properties at the atomic and molecular levels, since most experiments only provide macroscopic manifestations of the actual microscopic phenomena. This leads to a loss of crucial microscopic information. Even the most advanced experimental techniques such as the surface force apparatus provide only limited information. Therefore, the powerful tool of molecular simulation has largely been used to investigate the behavior of such confined systems as it has the advantage of providing more detailed and precise information at the microscopic level.

Molecular dynamics and Monte Carlo methods remain the favored choice in studying the properties of confined fluids.[5–10] To date there have been few molecular simulations of confined polymeric fluids under flow conditions. There have been several equilibrium and nonequilibrium molecular dynamics (NEMD) studies of confined alkanes under planar Couette flow that have studied the structure and rheology of such fluids,[10] and in some cases agreement with experimental measurement has been impressive.[11] Simulations of confined polymers are less common, but their number is growing. Varnik *et al.*[12] studied the pressure of polymeric thin films by molecular dynamics techniques and have applied their work to the study of supercooled thin polymer films[13]

[a]Present address: CSIRO Petroleum Resources, Ian Wark Laboratory, Bayview Avenue, Clayton, Victoria 3168, Australia.
[b]Author to whom correspondence should be addressed. Electronic mail: btodd@swin.edu.au

 © 2007 American Institute of Physics

Downloaded 30 Jun 2008 to 136.186.1.187. Redistribution subject to AIP license or copyright; see http://jcp.aip.org/jcp/copyright.jsp

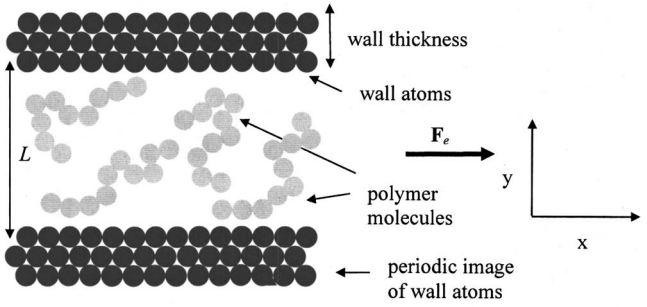

FIG. 1. Geometry of the overall simulation system including molecular fluid and wall atoms (z direction normal to page).

and investigations at the glass transition temperature.[14] Monte Carlo simulations of confined polymers have also been attempted giving good agreement with experimental studies of the molecular structure of nanoconfined polymers.[15] Langevin dynamics coupled with a simplified charged polymer model[16] has also been used to characterize the function of proteins, where chain length and net charge are found to be the dominating features that determine overall structure. Most work to date has been performed on linear chains, but some work is appearing in the literature specific to branched polymers.[17,18] It is clear that the field is still in its infancy and the number of simulation studies of confined complex fluids will most likely significantly increase in the future.

The goal of this study is to better understand the spatially dependent structural and dynamic properties for confined nonequilibrium polymeric fluids using NEMD. In particular, we study chain systems undergoing planar Poiseuille flow. The remainder of the manuscript is set out as follows. In Sec. II the computational methodology used in this work is described; in Sec. III we present the results and discuss them at length; finally in Sec. IV we form some conclusions.

II. COMPUTATIONAL METHODOLOGY

The systems studied in this work are confined polymeric fluids in slit pores (shown in Figs. 1 and 2). The coordinate system is chosen so that the wall surfaces lie in the x-z plane and the normal of the surface is in the y direction. Our geometry is such that $y=0$ defines the center of the fluid pore. A constant field drives the fluid in the x direction. Each wall is three atomic layers thick, and the second wall is just the periodic image of the first to allow greater computational efficiency. In previous work,[5] such a scheme was compared

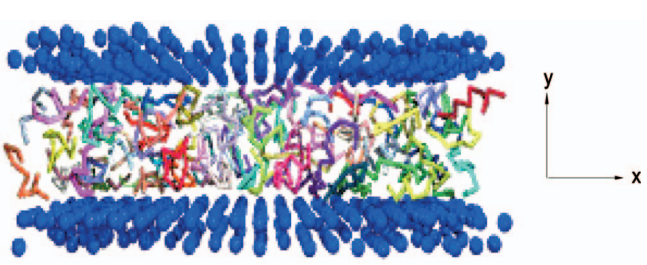

FIG. 2. (Color) Snapshot of the simulation. Blue particles represent the walls and the others confined between the walls are fluid molecules. z axis is normal to the page.

with a scheme in which two distinct walls confined the fluid, and all physical properties computed were identical within statistical errors. The effective pore width L is defined as the distance between the centers of mass of the two innermost opposing wall layers. The entire cell is thus periodic in x, y, and z. The walls are kept at a constant reduced temperature of 1.0 and density of 0.85 and are thermostated using a Gaussian constraint.[5] Unless otherwise stated, we consider average fluid atomic number densities of 0.45 and 0.65 in reduced units. The chain molecules between the walls are described by a bead-spring model. The advantage of such a simple model is that it has been shown to yield realistic dynamics for polymer melts.[19] Work has also been done to show how to map between it and detailed chemical models of polymers.[20,21]

Each molecule contains N_s spherical atoms of mass m. We consider chains with $N_s=2$, 4, 10, 20, and 50 "beads" per chain. All inter- and intra-atomic sites interact through the Weeks-Chandler-Andersen (WCA) potential,[22]

$$U^{\mathrm{WCA}}(r_{ij}) = \begin{cases} 4\varepsilon[(\sigma/r_{ij})^{12} - (\sigma/r_{ij})^{6}] - U^{\mathrm{LJ}}(r_c), & r_{ij} < r_c \\ 0, & r_{ij} \geqslant r_c, \end{cases} \tag{1}$$

where r_{ij} is the separation between the sites represented by atoms i and j, r_c is the truncation distance, $2^{1/6}\sigma$, ε is the potential well depth, σ is the effective diameter of the atomic sites, and $U^{\mathrm{LJ}}(r_c)$ is the unshifted Lennard-Jones potential evaluated at the truncation distance. In our simulations the wall and fluid atoms have the same Lennard-Jones parameters and the same masses. We give all quantities in terms of Lennard-Jones reduced units: reduced distance $r_{ij}^*=r_{ij}/\sigma$, density $\rho^*=\rho\sigma^3$, temperature $T^*=k_BT/\varepsilon$, energy $U^*=U/\varepsilon$, time $t^*=t/(\sigma\sqrt{m/\varepsilon})$, pressure $p^*=p\sigma^3/\varepsilon$, and strain rate $\dot{\gamma}^*=\sqrt{m\sigma^2/\varepsilon}\,\dot{\gamma}$. For simplicity of notation, hereafter the asterisk will be omitted. We set $\sigma=\varepsilon=m=1$.

Adjacent atoms along a chain are coupled by an additional potential that prevents chains from breaking or stretching indefinitely,

$$U^{\mathrm{FENE}}(r_{ij}) = -(1/2)kR_0^2 \ln[-(r_{ij}/R_0)^2], \quad r_{ij} \leqslant R_0, \tag{2}$$

where U_{ij}^{FENE} is an attractive finitely extensible nonlinear elastic (FENE) potential,[19] R_0 is a finite extensibility, and k is a spring constant. We set $R_0=1.5\sigma$ and $k=30\varepsilon/\sigma^2$. The choice of parameters for the FENE potential has been demonstrated to prevent bond crossing at temperatures even higher than the one used in our simulation.[19] We plot the two separate interatomic potentials, as well as their sum, in Fig. 3.

The fluid atoms obey Newton's equations of motion,

$$\dot{\mathbf{r}}_{i\alpha} = \frac{\mathbf{p}_{i\alpha}}{m_{i\alpha}}, \tag{3a}$$

$$\dot{\mathbf{p}}_{i\alpha} = \mathbf{F}_{i\alpha}^{\mathrm{WCA}} + \mathbf{F}_{i\alpha}^{\mathrm{FENE}} + \mathbf{i}m_{i\alpha}F_e, \tag{3b}$$

where $\mathbf{F}_{i\alpha}^{\mathrm{WCA}}$ is the WCA force exerted on atom α of molecule i due to all the other inter- and intramolecular fluid atoms and wall atoms and $\mathbf{F}_{i\alpha}^{\mathrm{FENE}}$ refers the FENE force exerted on atom α of molecule i due to intramolecular interac-

Downloaded 30 Jun 2008 to 136.186.1.187. Redistribution subject to AIP license or copyright; see http://jcp.aip.org/jcp/copyright.jsp

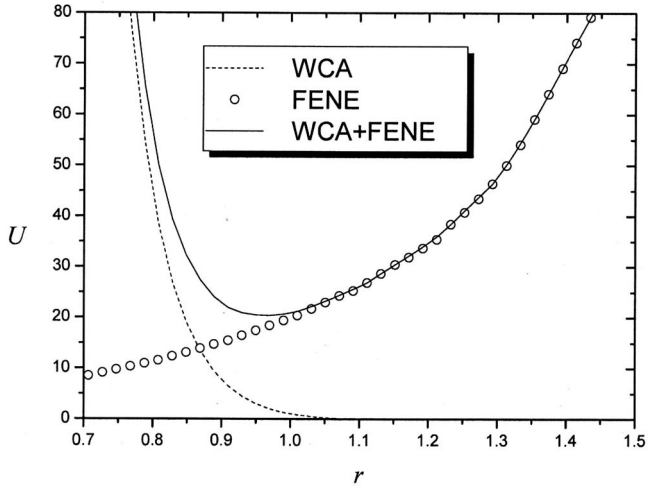

FIG. 3. Comparison of WCA, FENE, and WCA+FENE potentials.

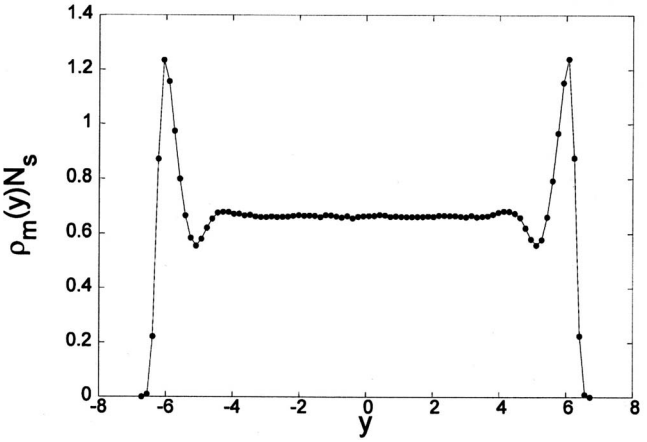

FIG. 4. Fluid molecular number density $\rho_m(y)$ multiplied by the number of atoms N_s per chain for an average fluid density of $\rho=0.65$, external field $F_e=0.05$, molecular length of $N_s=4$, and pore width $L=14.0$.

tions governed by the additional FENE potential. F_e is the external driving field per unit mass and $\mathbf{i}$ is the unit vector in the x direction. The field F_e is equivalent to a gravitational-like field and its relation to a constant pressure gradient in the case of Poiseuille flow has been described in detail in Ref. 5. Here $\mathbf{r}_{i\alpha}$ and $\mathbf{p}_{i\alpha}$ refer to the laboratory position and momentum of site α on molecule i, respectively. Note that the equations of motion for the fluid do not include a thermostat term and energy is dissipated only through the thermostated walls, leading to essentially quartic temperature profiles typically associated with Poiseuille flow.[8] The equations of motion for wall atoms are as given previously.[5,23] In our simulations we use the field strength of $F_e=0.05$ which yields a fluid temperature of 1.0.

The equations of motion are solved with a fifth order Gear predictor-corrector scheme with an integration time step of $\tau=0.001$. Our simulations are first run for a total of $\sim 10^6$ time steps to reach a nonequilibrium steady state. Once steady state is achieved, typical production runs of a total of 50×10^6 time steps are run with averages accumulated in blocks of 10^6 time steps.

III. SIMULATION RESULTS

A. Validation

In order to validate our simulation results, we first simulate a fluid composed of molecules undergoing planar Poiseuille flow between two atomistic walls. The simulation conditions are similar to those used by Travis and Evans.[24] Our results qualitatively agree with their work.

The atomic number density $\rho_a(\mathbf{r},t)$ and molecular number density $\rho_m(\mathbf{r},t)$ at position $\mathbf{r}$ and time t are defined by

$$\sum_{i=1}^{N_m}\sum_{\alpha=1}^{N_s} m_{i\alpha}\delta(\mathbf{r}-\mathbf{r}_{i\alpha}(t)) \equiv m\rho_a(\mathbf{r},t), \tag{4}$$

$$\sum_{i=1}^{N_m} M_i\delta(\mathbf{r}-\mathbf{r}_i^c(t)) \equiv M\rho_m(\mathbf{r},t), \tag{5}$$

where N_m is the number of fluid molecules, N_s is the number of atomic sites per molecule, the index i labels the individual molecules, α labels the particular atomic site in molecule i, $\mathbf{r}_{i\alpha}(t)$ is the position vector of site α in molecule i at time t, and $\mathbf{r}_i^c(t)$ is the center of mass position of molecule i at time t. Fluid atoms are assumed here to have identical masses, $m_{i\alpha}=m$, and M is the mass of a fluid molecule $(M=mN_s)$.

Similarly, the atomic streaming velocity $\mathbf{u}_a$ and molecular streaming velocity $\mathbf{u}_m$ are defined as follows:

$$\mathbf{u}_m(\mathbf{r},t) = \frac{\sum_{i=1}^{N_m} M\mathbf{v}_i^c(t)\delta(\mathbf{r}-\mathbf{r}_i^c(t))}{\sum_{i=1}^{N_m} M\delta(\mathbf{r}-\mathbf{r}_i^c(t))}, \tag{7}$$

where $\mathbf{v}_{i\alpha}(t)$ is the velocity of site α on molecule i at time t. $\mathbf{v}_i^c(t)$ is the center of mass velocity of fluid molecule i at time t. For a system such as ours we divide the simulation cell into a number of bins of thickness Δy and compute the number density and streaming velocity as an average evaluated at the midpoint of each bin. This is the simple histogram method. In order to be compared with the atomic number density profile, the molecular number density is multiplied by the number of atoms N_s per chain. In Fig. 4 we plot the molecular number density $\rho_m(y)$ multiplied by the number of atoms N_s per chain for an average fluid density of $\rho=0.65$, external field $F_e=0.05$, molecular length of $N_s=4$, and pore width $L=14.0$. As is to be expected the fluid experiences large density oscillations particularly in the layers immediately adjacent to both walls. These oscillations become less significant towards the center of the pore. Significant inhomogeneity appears only in the immediate vicinity of the walls.

The molecular streaming velocity profile is displayed in Fig. 5. For a classical Navier-Stokes fluid undergoing planar Poiseuille flow the streaming velocity profile should be quadratic in y. We can see near the center of the pore that the streaming velocity profile is close to the quadratic profile, but deviations from the classical Navier-Stokes prediction are significant close to the interface between wall and fluid molecules. Abrupt changes in the streaming velocity close to the walls indicate slip boundary conditions.

If $\mathbf{S}_b$ is the total intrinsic angular momentum of molecules in a bin and $\boldsymbol{\omega}$ is the streaming angular velocity in that bin then

Downloaded 30 Jun 2008 to 136.186.1.187. Redistribution subject to AIP license or copyright; see http://jcp.aip.org/jcp/copyright.jsp

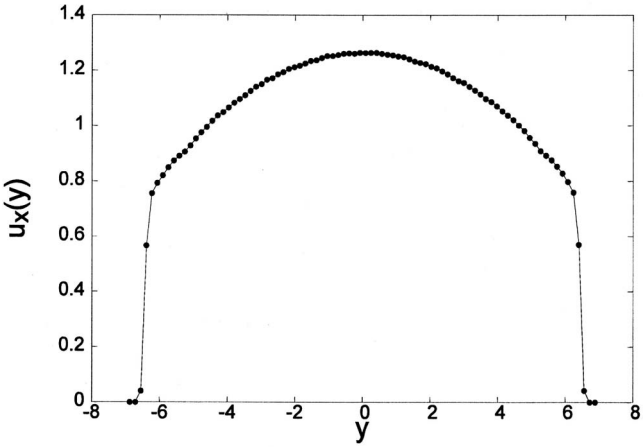

FIG. 5. Streaming velocity $u_x(y)$ as a function of y for the same system as Fig. 4.

$$\mathbf{S}_b = \mathbf{\Theta}_b \cdot \boldsymbol{\omega}, \tag{8}$$

where

$$\mathbf{S}_b = \sum_{i \in \text{bin}} \sum_{\alpha} \mathbf{r}'_{i\alpha} \times \mathbf{p}_{i\alpha},$$

$$\mathbf{\Theta}_b = \sum_{i \in \text{bin}} \mathbf{\Theta}_i, \tag{9}$$

and

$$\mathbf{\Theta}_i = \sum_{\alpha \in i} m(r'^2_{i\alpha}\mathbf{l} - \mathbf{r}'_{i\alpha}\mathbf{r}'_{i\alpha})/M \tag{10}$$

is the moment of inertia tensor per unit mass of molecule i and $\mathbf{l}$ is the unit tensor. The index α labels the atomic sites in molecule i and $\mathbf{r}'_{i\alpha}$ is the vector from the center of mass of molecule i to site α of the same molecule.

We compute the streaming angular velocity by solving Eq. (8). In Fig. 6 we show the x, y, and z components of the streaming angular velocity for an average fluid density of $\rho = 0.65$, external field $F_e = 0.05$, molecular length of $N_s = 4$, and pore width $L = 14.0$. ω_x and ω_y are zero as expected, and ω_z is a linear function of y away from the walls. In Fig. 6(c) we also plot $1/2\nabla \times \mathbf{u}$, one half the vorticity. Sarman and Evans[25] proved that for homogeneous systems, in the absence of external applied torques, $\boldsymbol{\omega} = 1/2\nabla \times \mathbf{u}$. For our geometry this reduces to $\omega_z = -(1/2)\dot{\gamma}$, where $\dot{\gamma} \equiv \partial u_x(y)/\partial y$ is the strain rate. Away from the walls this relation holds for our system. The streaming velocity shown in Fig. 5 and ω_z in Fig. 6(c) qualitatively agree with the results obtained by Travis and Evans.[24] They do not agree quantitatively because Travis and Evans simulated dimers with rigid bond constraints, whereas our chains are four-site chains modeled with the more flexible FENE potential.

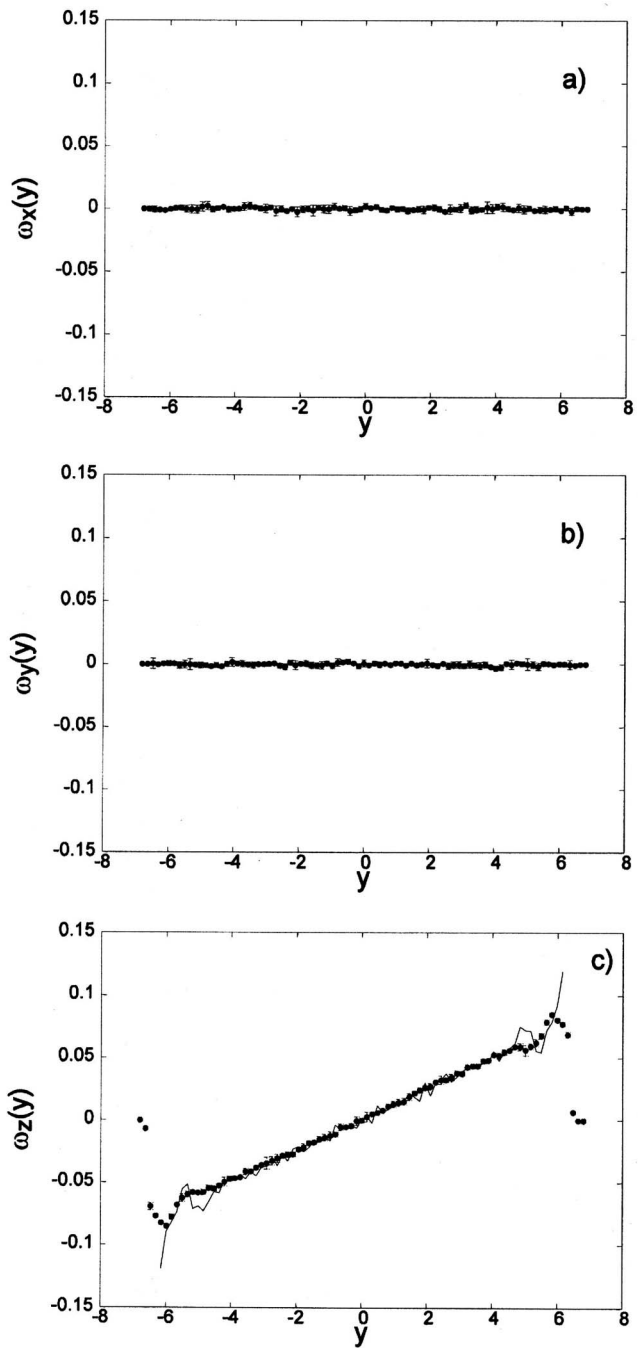

FIG. 6. Components of the streaming angular velocity for the system specified in Fig. 4. (a) x component ω_x; (b) y component ω_y; and (c) z component ω_z (filled circles) and one half the vorticity, $1/2\nabla \times \mathbf{u}$ (solid line).

B. Atomic and molecular number density profiles

Probably the most interesting static properties in confined systems concern the shape and size of the chains in the vicinity of the surfaces and how they deviate from the respective bulk shape and sizes. The most appropriate quantities to describe these are the radius of gyration of the chain and the atomic and molecular density profiles across the pore. In Fig. 7, we plot the atomic and molecular number densities for the indicated chain lengths for an average fluid density of $\rho = 0.65$, external field $F_e = 0.05$, and pore width $L = 7.0$. In order to be compared with the atomic number density profile, the molecular density is multiplied by the number of atoms N_s per chain. The influence of the chain length on the atomic number density is minimal as shown in Fig. 7(a). The molecular number density shown in Fig. 7(b) depends much more strongly on the chain length. For $N_s = 2$, the high density next to the wall is followed by a density depletion layer and then a second density peak. Alternating

Downloaded 30 Jun 2008 to 136.186.1.187. Redistribution subject to AIP license or copyright; see http://jcp.aip.org/jcp/copyright.jsp

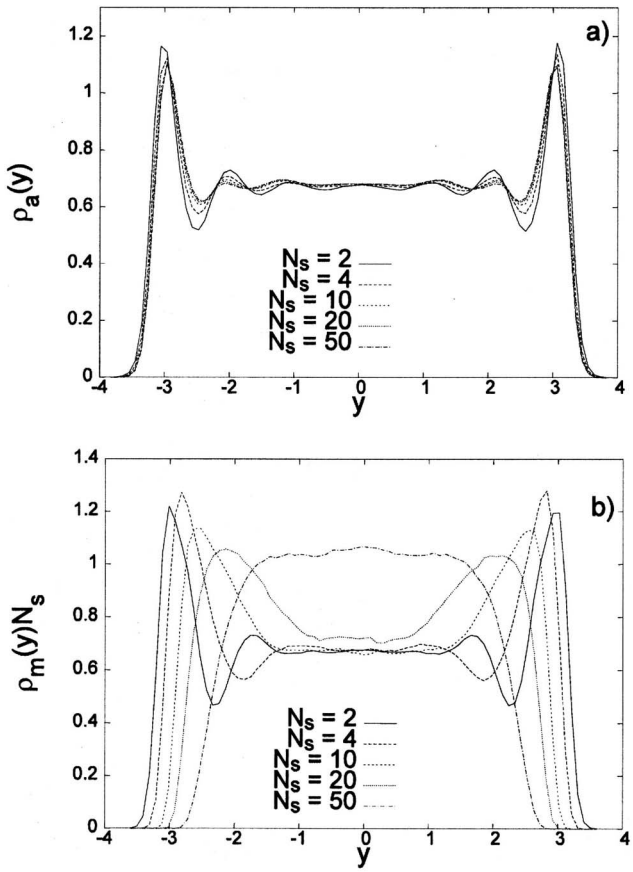

FIG. 7. (a) Atomic number density $\rho_a(y)$ and (b) molecular number density $\rho_m(y)$ multiplied by the number of atoms N_s per chain for an average fluid density of $\rho=0.65$, external field $F_e=0.05$, and pore width $L=7.0$.

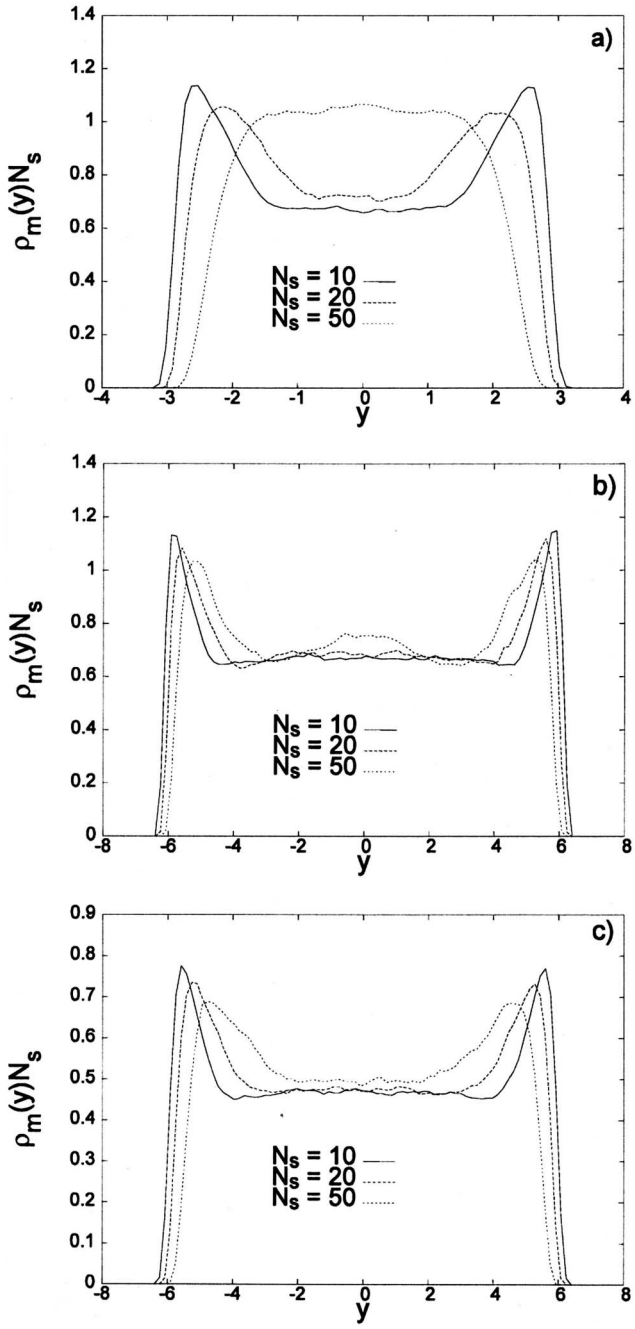

FIG. 8. Comparison of molecular number density $\rho_m(y)$ multiplied by the number of atoms N_s per chain for average fluid densities of $\rho=0.45$ and $\rho=0.65$, external field $F_e=0.05$, and molecular lengths of $N_s=10$, 20, and 50. (a) $\rho=0.65$ and $L=7$; (b) $\rho=0.65$ and $L=14.0$; and (c) $\rho=0.45$ and $L=14.0$.

density minima and maxima are developed across the fluid pore. This oscillatory layering effect is also observed in equilibrium molecular dynamics simulations of *n*-alkane melts (for example, see Ref. 26 and references therein), and it has been shown that it depends strongly on the detailed interaction potential between the wall and the fluid. In Fig. 7(b) the maximum peak is around 1.9 times larger than the bulk density which is in agreement with what is reported for the equilibrium case, where the wall and fluid interactions are the same as that in the fluid.[27] The layered structure is more obvious if the chain length is small compared to the size of the pore. By constraining the atoms in chains, an extra entropic cost is introduced and this entropy loss scales as $N_s^{1/2}$.[28] As the decrease of the layering further away from the walls is of an entropic nature, it would be expected that with increasing chain length this entropic cost would increase. As a result, for the larger chain lengths of $N_s=10$, 20, and 50 compared with $N_s=4$ we observe the decrease of the first layer in the molecular number density profile. As is physically plausible, the location of the first peak of the molecular density profile shifts towards the center of the pore as the chain length increases. The molecular number density does not follow the atomic layering, since atoms in the first atomic layer have their center of mass of the molecular chain in the region of the depletion zone between the first and the second atomic layers.

In Fig. 8 we present the comparison of molecular number densities for three different molecular lengths of $N_s=10$, 20, and 50, average fluid densities of $\rho=0.45$ and 0.65, external field $F_e=0.05$, and pore widths of $L=7.0$ and 14.0. It can be seen that the layered structure is more obvious for the smaller chain lengths, which is the direct result of its entropic nature. For the wider pore the molecular number density is almost constant in the central pore region, seen in Figs. 8(b) and 8(c).

C. Extension of molecules

A polymer molecule can exist in many different configurations due to many internal degrees of freedom. Two impor-

Downloaded 30 Jun 2008 to 136.186.1.187. Redistribution subject to AIP license or copyright; see http://jcp.aip.org/jcp/copyright.jsp

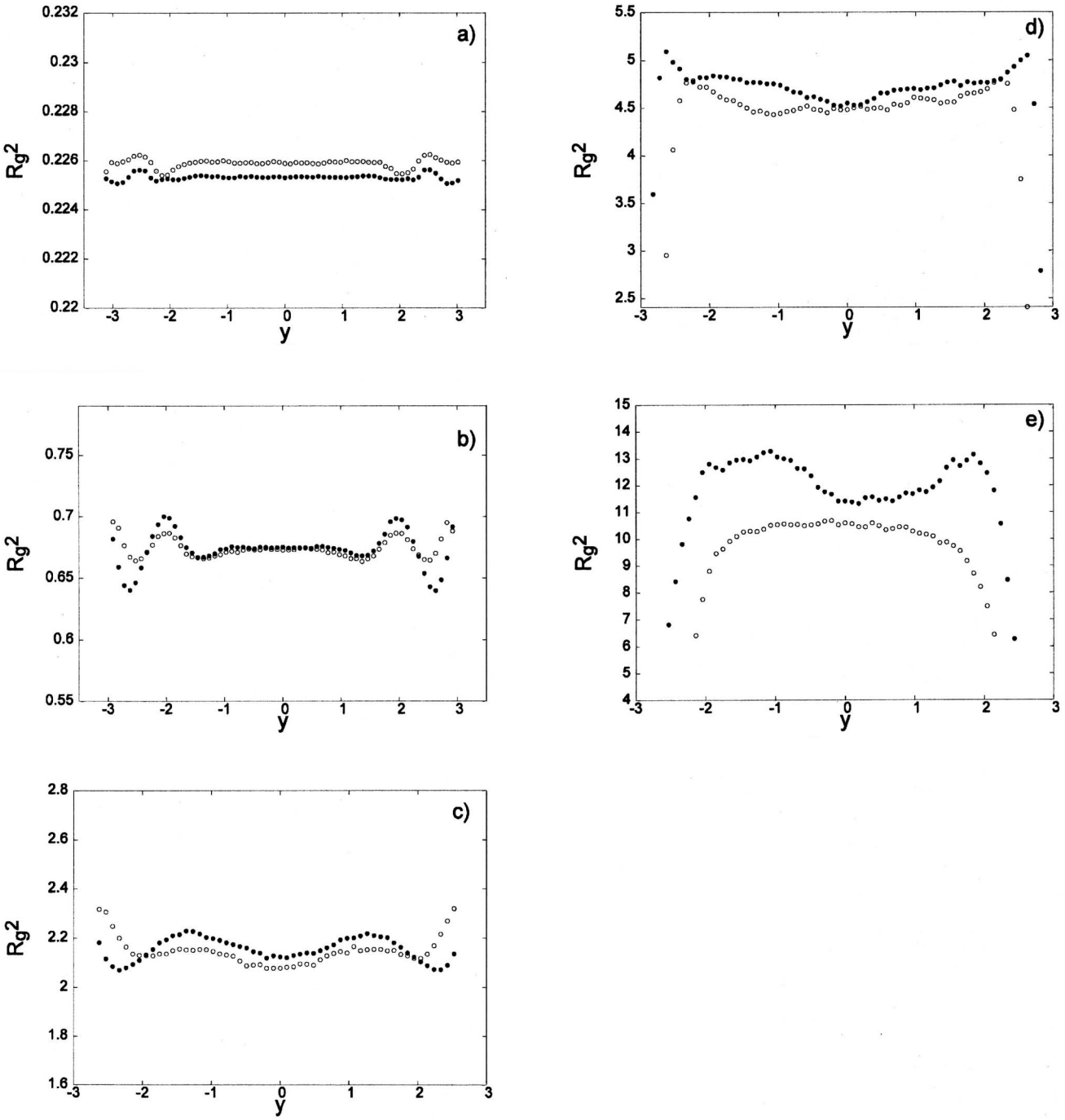

FIG. 9. Mean squared radius of gyration as a function of y for average fluid densities of $\rho=0.45$ (circles) and $\rho=0.65$ (filled circles), external field $F_e=0.05$, and pore width $L=7.0$. (a) $N_s=2$; (b) $N_s=4$; (c) $N_s=10$; (d) $N_s=20$; and (e) $N_s=50$.

tant parameters used to measure the configuration of linear polymers are the average end-to-end distance R_e, proportional to $N_s^{1/2}$ in the melt and related to the polymer size, and the radius of gyration R_g, which is a measure of the distribution of beads in the polymer chain.[29] For ideal (Gaussian) chains we have $R_e^2=N_sb^2$ and $R_g^2=\frac{1}{6}N_sb^2$, where b is the bond length. Thus, for an ideal chain the ratio of R_e^2 to R_g^2 is the constant value of 6.

In order to quantify the extension of the confined molecules, we divide the space between the two walls into slices and for each slice the mean squared radius of gyration and the mean squared end-to-end distance are computed as an average evaluated at the midpoint of each slice. In Figs. 9 and 10 we show the mean squared radius of gyration R_g^2 and the mean squared end-to-end distance R_e^2 as a function of y for average fluid densities of $\rho=0.45$ and $\rho=0.65$, external field $F_e=0.05$, pore width $L=7.0$, and molecular lengths of $N_s=2$, 4, 10, 20, and 50. Our results show that R_g^2 and R_e^2 for $N_s=2$ are roughly constants while there are substantial variations for $N_s=4$, 10, 20, and 50. The reason for this is that for two-site molecules the center of mass of each molecule can only change by bond stretching as there is only one possible

Downloaded 30 Jun 2008 to 136.186.1.187. Redistribution subject to AIP license or copyright; see http://jcp.aip.org/jcp/copyright.jsp

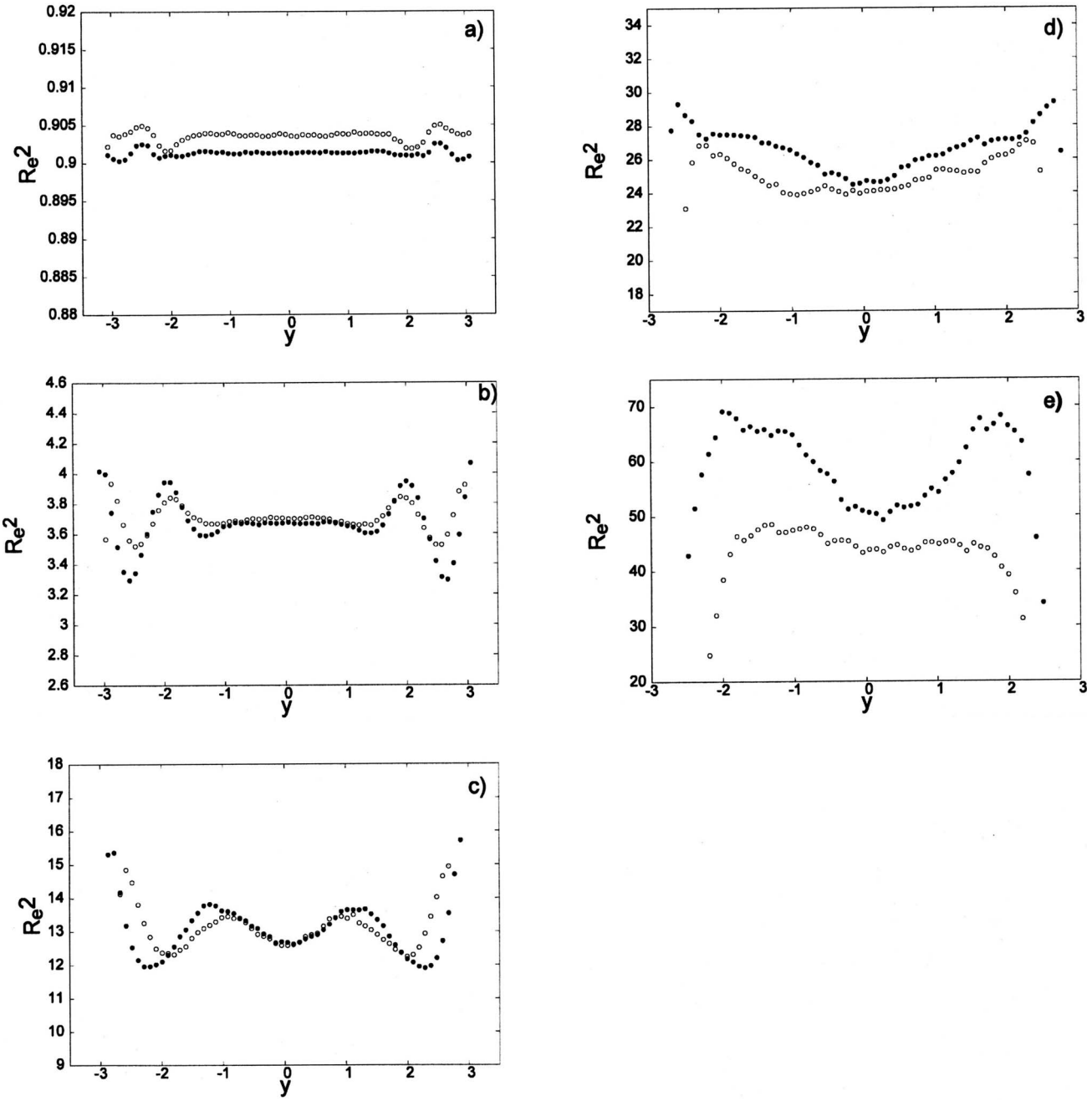

FIG. 10. Mean squared end-to-end distance as a function of y for average fluid densities of $\rho=0.45$ (circles) and $\rho=0.65$ (filled circles), external field $F_e=0.05$, and pore width $L=7.0$. (a) $N_s=2$; (b) $N_s=4$; (c) $N_s=10$; (d) $N_s=20$; and (e) $N_s=50$.

configurational state. However, for molecules of $N_s=4$, 10, 20, and 50, the configurations of the molecules are changed, and the centers of mass of the molecules locate outside of the molecular chains, as depicted in Fig. 11.

A decrease in the mean squared radius of gyration reflects the shrinkage of molecules which might result from the increase in the molecular number density. On the other hand, an increase in the mean squared radius of gyration indicates the expansion of molecules due to the decrease in the molecular number density. For the given values of the pore size, external force, and chain length, decreases in the maximum values of R_g^2 and R_e^2 with increasing average fluid density indicate that the stretching of the molecules decreases as the density of packing prevents molecules from expansion. As is to be expected, for $N_s=2$ and 4 and pore width of $L=7.0$, both R_g^2 and R_e^2 experience strong oscillations which decay in strength towards the center of the pore. As the length of the molecule exceeds the width of the channel it is more ener-

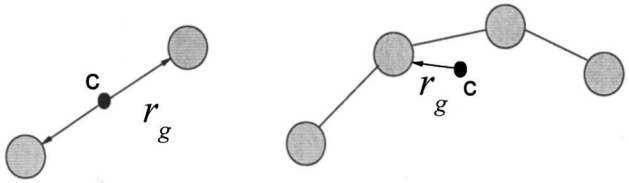

FIG. 11. Schematic representation of the configurations of the two-site and four-site chain molecules. $\boldsymbol{C}$ is the center of mass of each molecule.

Downloaded 30 Jun 2008 to 136.186.1.187. Redistribution subject to AIP license or copyright; see http://jcp.aip.org/jcp/copyright.jsp

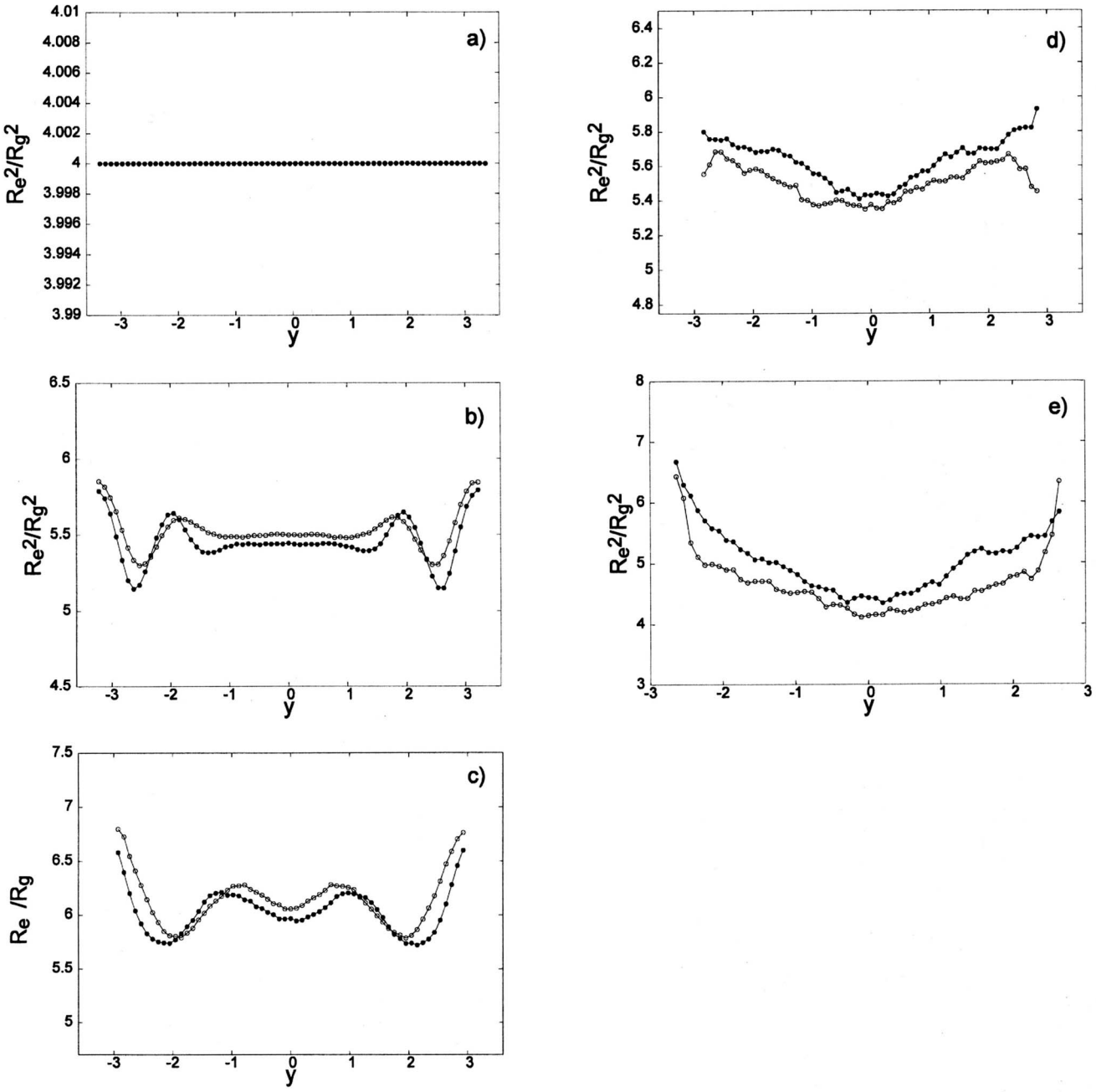

FIG. 12. Ratio of the mean squared end-to-end distance to the mean squared radius of gyration as a function of y for average fluid densities of $\rho=0.45$ (circles) and $\rho=0.65$ (filled circles), external field $F_e=0.05$, and pore width $L=7.0$. (a) $N_s=2$; (b) $N_s=4$; (c) $N_s=10$; (d) $N_s=20$; and (e) $N_s=50$. The lines serve as a guide to the eye.

getically favorable for the molecules in the dense system compared to the dilute system to unfold parallel to the wall, thereby increasing the end-to-end distances. This unfolding and layering is associated with an entropy cost. In the dilute situation this effect is not as pronounced since the restrictions due to inter- and intramolecular interactions are smaller. This explains the higher maximum value of R_g^2 and R_e^2 for the high density fluid and large N_s. The observed alignment of the polymers with the wall is also observed in equilibrium simulations of *n*-alkanes.[26] Moreover, in the equilibrium situation the degree of alignment is shown to exhibit oscillations near the wall interface which is in agreement with the results in Figs. 9 and 10.

At the wall we observe a dramatic drop in both the end-to-end distance and the radius of gyration (for $N_s=20$ and 50). This is due to the fact that the density of the melt increases at the wall-fluid boundary. It is interesting to note that increasing the field strength sufficiently results in a qualitatively different behavior: the end-to-end distance and the radius of gyration will increase at the boundary. The reason for this is that the large external field forces the molecules to align parallel to the walls, stretching the innermost molecules by up to 20% of the maximum length (not shown in the figures).

In Fig. 12 we plot the ratio of the mean squared end-to-end distance to the mean squared radius of gyration as a

Downloaded 30 Jun 2008 to 136.186.1.187. Redistribution subject to AIP license or copyright; see http://jcp.aip.org/jcp/copyright.jsp

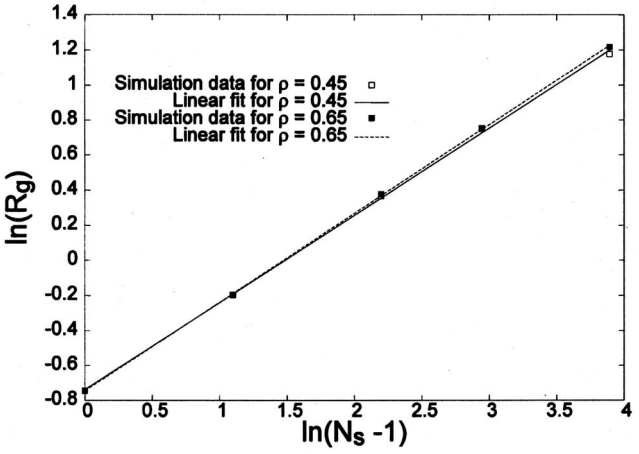

FIG. 13. Logarithm of average radius of gyration at the center of fluid pore $\ln(R_g)$ vs the logarithm of the number of bonds per chain $\ln(N_s-1)$. The squares represent simulation results for average fluid density of $\rho=0.45$ and the filled squares are the results for $\rho=0.65$. Also shown are the linear fits to the data, where the full line is the fit for $\rho=0.45$ and the dashed line is for $\rho=0.65$. The external field is 0.05 and pore width $L=7.0$. The linear fit gives $R_g=AN_b^{\nu}$, where $\nu=0.498\pm0.001$ for $\rho=0.45$ and $\nu=0.508\pm0.002$ for $\rho=0.65$.

function of y for $N_s=2$, 4, 10, 20, and 50 for average fluid densities of $\rho=0.45$ and $\rho=0.65$, external field $F_e=0.05$, and pore width $L=7.0$. It can be seen that for $N_s=2$ and 4, the ratios are less than 6, the theoretical value of the ratio for ideal chains as discussed earlier.[29,30] For $N_s=10$ the ratios fluctuate around 6. For large chains, especially for $N_s=50$, the ratios deviate from the theoretical prediction for the ideal chains as a result of chain unfolding parallel to the walls. It should be stressed that the molecular theories on chain statistics are valid only for homogeneous equilibrium systems. The ideal chain model takes into account the short range interactions between beads which are located close to each other along the chain by redefining the bond length as an effective bond length. The beads of the Lennard-Jones chains used in this work cannot overlap each other due to the Lennard-Jones potential which is strongly repulsive at short distances. Therefore there exist regions of excluded volume in these chains. The average size of an excluded volume chain is larger than the ideal chain of the same length, as the restriction that no overlapping is permitted would result in the larger value of size distribution.

The statistical properties of excluded volume chains have been extensively investigated, and for large N_s it has been found that the size obeys the relationship[29,31] $R_g=AN_b^{\nu}$, where N_b is the number of bonds in the chain given as $N_b=N_s-1$. The prefactor A is model dependent, whereas the exponent ν is very close to the value of 0.588 for chains in a good solvent and 0.5 for a melt at equilibrium.[29] In Fig. 13 we plot the logarithm of the average radius of gyration at the center of the fluid pore versus the logarithm of the number of bonds per chain for $\rho=0.45$ and 0.65. It is clear that the power law is fulfilled in the case of nonequilibrium flows, provided that the external field is kept sufficiently low. The fits of the data yield exponents $\nu=0.498\pm0.001$ for $\rho=0.45$ and $\nu=0.508\pm0.002$ for $\rho=0.65$ which resemble the results from the corresponding equilibrium simulation. It is worth noting that the property $\nu=0.5$ is only expected for relatively large N_s; nevertheless, we also observe this for low N_s. If the external field is increased ν increases indicating a stretching of the molecule under shear.[32]

D. Streaming velocity, strain rate, and shear stress

The molecular streaming velocity profiles are displayed in Fig. 14 for average fluid densities of $\rho=0.45$ and 0.65, external field $F_e=0.05$, pore widths $L=7.0$ and 14.0, and chain lengths $N_s=2$, 20, and 50. For fixed pore width, force strength, and chain length, the streaming velocity decreases with increasing average fluid density. This is due to increased resistance from surrounding molecules as the average fluid density increases. Contrasting these streaming velocity profiles with those for atomic fluids,[33] we observe what appears like the onset of pluglike flow, constant velocity of flow for the confined polymeric fluids for $N_s=20$ and 50, particularly for the higher density fluids. As the molecular length increases for any particular pore width, the strain rate in the middle of the pore is close to zero and the velocity gradients are strong near the walls but weak elsewhere, shown in Fig. 15. Pluglike flow occurs when the Reynolds number (in our case defined as $\rho u_x L/\eta$) is small, i.e., the ratio of inertial to viscous forces is low, and when there exists some degree of slip. As the viscosity of the fluid increases for a particular pore size (either due to higher average density or larger chain length) we might expect plug flow to occur if there is sufficient slip. For the $N_s=2$ systems [Figs. 14(a) and 14(d)], we observe that the fluid displays a typical quadratic Poiseuille flow profile away from the walls and the higher density fluid shows a flatter velocity profile. Similarly, for the $N_s=20$ and 50 systems [Figs. 14(b), 14(c), 14(e), and 14(f)], both densities display almost pluglike flow behavior away from the walls. In this case the viscosities of the $N_s=20$ and 50 polymer fluids are larger than the viscosity of the $N_s=2$ system, because it is well known that for low molecular weight polymers the viscosity scales as $\eta \propto N_s$ for a homogeneous fluid.[34] This has been confirmed by a number of independent NEMD simulation studies.[35] However, since the fluid streaming velocity adjacent to the wall is very low in all cases the degree of slip is very small or negligible for the systems studied here. Despite this, the velocity profiles are qualitatively similar to those obtained in actual experimental measurements of high density polyethylene in a slit die[36] where plug-flow behavior was observed with variable degrees of slip. The degree of slip is largely determined by the wall roughness, chain length, and wetting effects which explicitly depend on the wall-fluid and fluid-fluid interactions. For *n*-hexadecane Schmatko *et al.*[37] have shown experimentally that slippage exists for all contact angles including zero, i.e., even for highly attractive walls. Also, it must be mentioned that the slippage is observed for much lower applied external force. To our knowledge, no satisfactory theoretical description of this microscopic slippage is yet available.

In Figs. 14(b), 14(e), and 14(f) we clearly observe that the streaming velocity has two maxima away from the channel midpoint. This contradicts the fact that the molecular

Downloaded 30 Jun 2008 to 136.186.1.187. Redistribution subject to AIP license or copyright; see http://jcp.aip.org/jcp/copyright.jsp

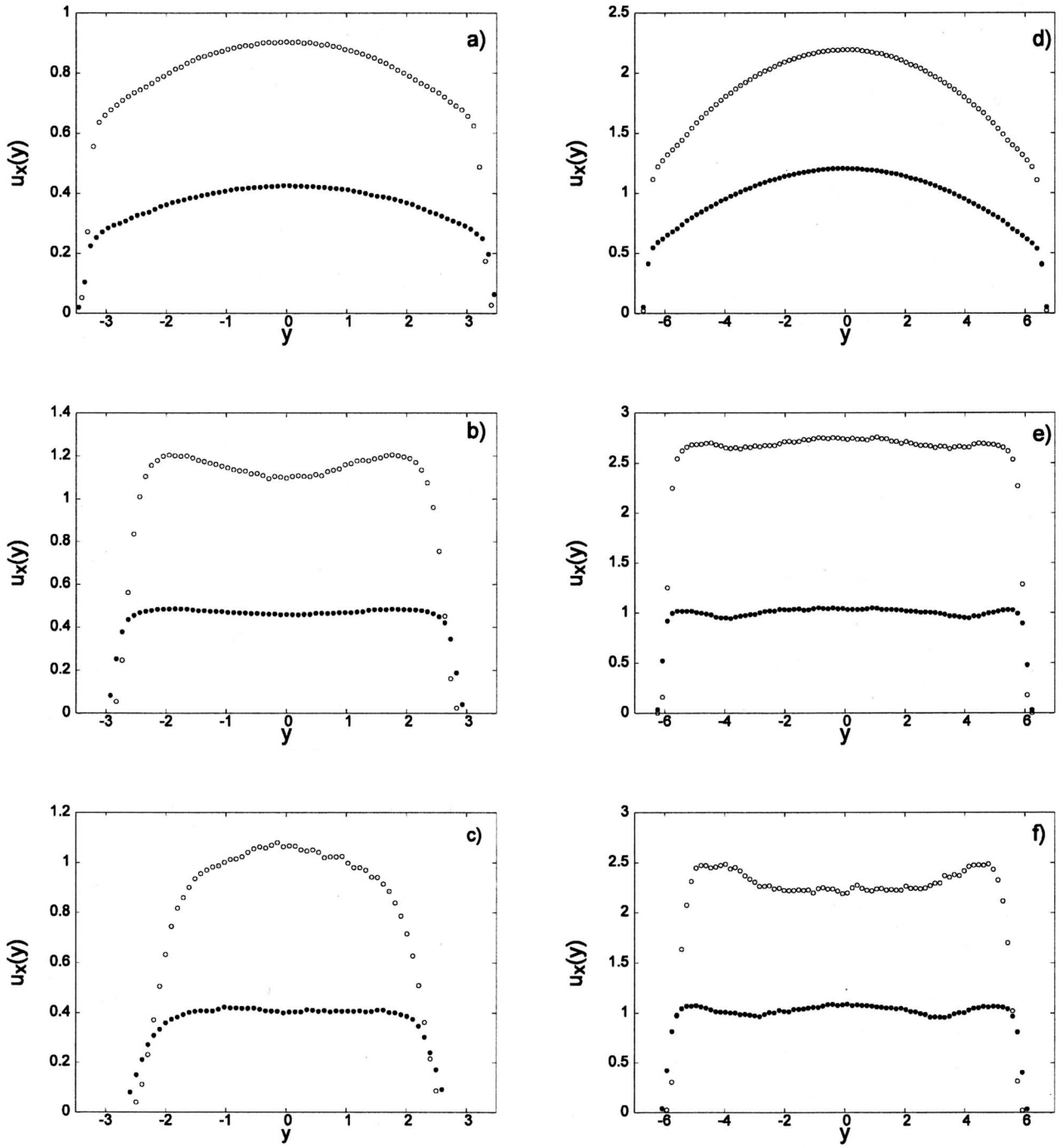

FIG. 14. Molecular streaming velocity as a function of y for average fluid densities of $\rho=0.45$ and 0.65 and external field $F_e=0.05$. (a) $N_s=2$, $L=7$; (b) $N_s=20$ and $L=7$; (c) $N_s=50$ and $L=7$; (d) $N_s=2$ and $L=14$; (e) $N_s=20$ and $L=14$; and (f) $N_s=50$ and $L=14$.

density is high in these areas which should increase the local fluid viscosity. However, from Figs. 9 and 10 we see that these maxima are correlated with relatively high end-to-end distances and radius of gyration; that is, there exists an alignment in the fluid in this region which decreases the viscosity. To complicate things even further, nonlocal viscous effects may also play an important role in the spatial variations of the fluid viscosity,[33,38,39] but we do not pursue this further here.

A closer examination of the streaming velocity profiles displayed in Fig. 14 shows that the flow near the midpore region is actually weakly quadratic, as seen in Fig. 16, where the velocity is plotted for the $L=14.0$, $\rho=0.65$, and $N_s=20$ system of Fig. 14(e) away from the walls. This weakly quadratic/pluglike behavior is probably due to there being few molecular layers of melt [see Figs. 8(a) and 8(b)] in the pore. This hinders the establishment of strongly quadratic fluid velocity profiles which would require more layers. This layering effect has been observed for highly confined atomic fluids[7] in which typical quadratic velocity profiles are destroyed but is likely to be more pronounced for chain molecules because of the additional topological constraints. This

Downloaded 30 Jun 2008 to 136.186.1.187. Redistribution subject to AIP license or copyright; see http://jcp.aip.org/jcp/copyright.jsp

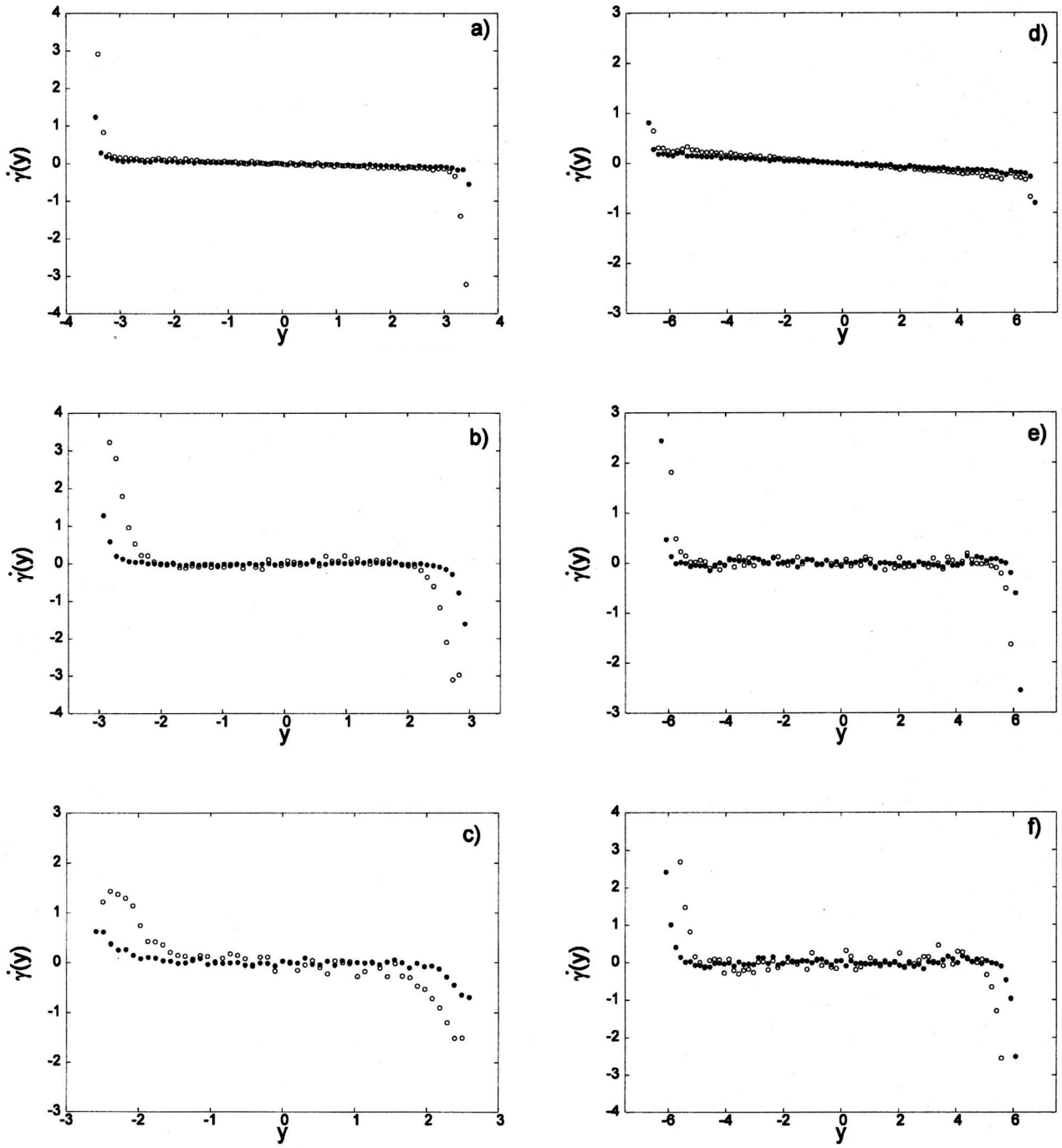

FIG. 15. Strain rate as a function of y for average fluid densities of $\rho=0.45$ and 0.65 and external field $F_e=0.05$. (a) $N_s=2$ and $L=7$; (b) $N_s=20$ and $L=7$; (c) $N_s=50$ and $L=7$; (d) $N_s=2$ and $L=14$; (e) $N_s=20$ and $L=14$; and (f) $N_s=50$ and $L=14$.

would tend to flatten out the velocity profiles when the chain length is comparable to or greater than the pore width.

In Fig. 17 we plot the negative of the molecular and atomic shear stresses as a function of y for the higher density, small pore system for all chain lengths. Both stresses are computed by the so-called IMC method[5] in which the relevant continuity equation for the atomic or molecular momentum density is integrated. In the case of the atomic shear stress, the atomic number density is integrated, whereas for the molecular stress the molecular number density times the number of beads (equivalent to the molecular mass density) is integrated. For a homogeneous system at steady state the two stresses should be identical. That they are different for our system is to be expected. It has been shown[40] that the continuity equation for the molecular momentum density is correct only to second order in the spatial gradients, unlike the continuity equation for the atomic momentum density which is exact. Since our system has large spatial gradients (see, for example, Fig. 7) it is to be expected that the molecular pressure computed by integrating the continuity equation for the molecular momentum density will be incorrect.

As can be seen in Fig. 17(b) the atomic stresses are all linear, upon which are superposed oscillations correlated with the atomic density (i.e., integration of an oscillating

Downloaded 30 Jun 2008 to 136.186.1.187. Redistribution subject to AIP license or copyright; see http://jcp.aip.org/jcp/copyright.jsp

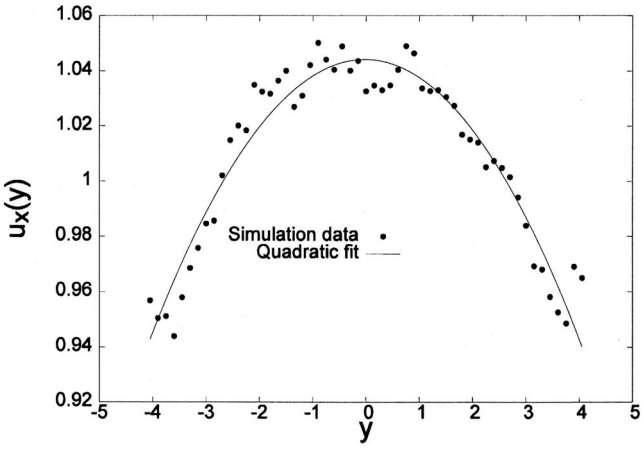

FIG. 16. Velocity profile for $\rho=0.65$, $N_s=20$, and $L=14$ in the midpore region.

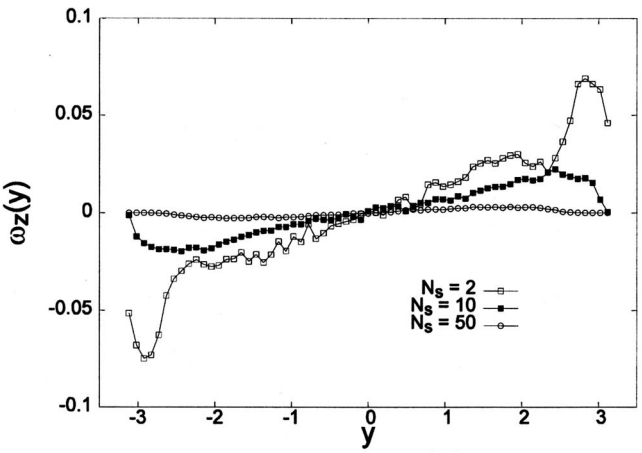

FIG. 18. z components of the streaming angular velocity for an average fluid density of $\rho=0.65$, external field $F_e=0.05$, and pore width $L=7.0$. The lines serve as guide to the eye.

density profile will result in an oscillating shear stress profile). The stresses are largely independent of chain length as indeed could be inferred by noting that the atomic density profiles for all chains are very similar for the state point and field strength in question [see Fig. 7(a)]. In principle we could compute an effective pore viscosity by using Newton's viscosity law applied locally ($\bar{\eta}=-P_{yx}/\dot{\gamma}$), where the stress and strain rate are evaluated near the center of the pore. However, for our systems this would lead to very large statistical uncertainties because the pluglike flow behavior results in velocity gradients that are close to zero in this region. Evaluating a local viscosity near the walls where the velocity gradients are large will almost certainly result in significant error because this is the region where nonlocal viscous effects dominate.[33,38,39]

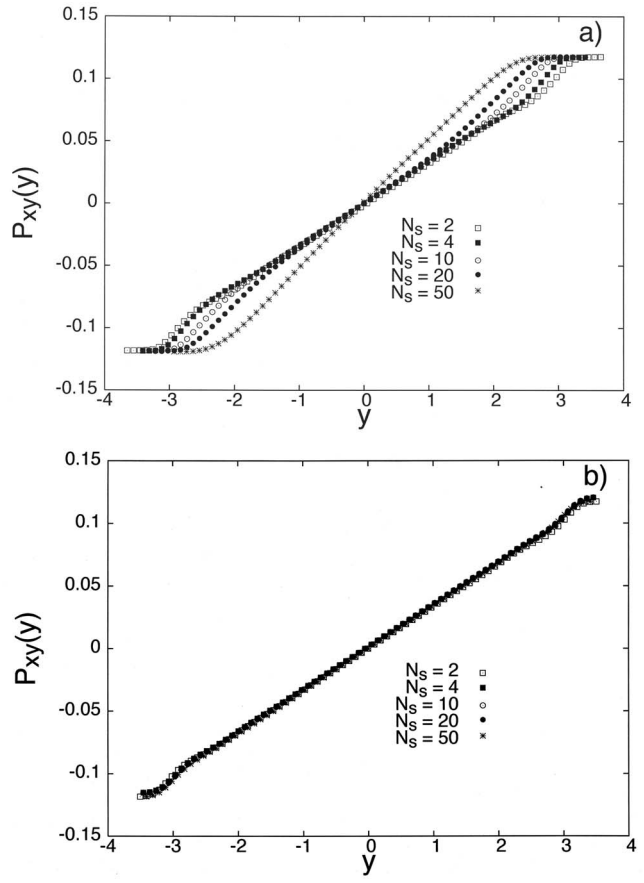

FIG. 17. Negative shear stress $[P_{yx}(y)]$ as a function of y for the system $\rho=0.65$, $F_e=0.05$, $L=7.0$, and molecular lengths $N_s=2$, 4, 10, 20, and 50. (a) Molecular shear stress; (b) atomic shear stress.

E. Molecular rotation

The streaming angular velocity of the polymers is determined by Eq. (8). Figure 18 shows a plot of the z component of the streaming angular velocity as a function of y for the indicated chain lengths for the narrower pore. The magnitude of ω_z decreases as the chain length increases for the given values of the overall system density and external field. Note that for the largest chain length, $N_s=50$, there is no freedom for the molecule to rotate at all anywhere in the pore and ω_z is close to zero everywhere. The rotation of molecules depends on two factors: the value of the velocity gradient at the center of mass location and its radius of gyration compared to the pore width. For our confined fluids under Poiseuille flow, rotation requires both sufficiently large velocity gradients and adequate available space to rotate. For chains with sufficiently small R_g, rotation is strongest near the wall boundaries because this is where the velocity gradients are strongest. Near the center of the pore all chains have small ω_z that are identically zero at the pore center $(y=0)$ where the velocity gradient is zero. The individual chains of the $N_s=50$ system are sufficiently large such that $R_g>L$ for the $L=7.0$ system; thus no molecular rotation can occur anywhere.

In Fig. 19 we plot the z component of the streaming angular velocity (filled circles) and one half the vorticity (line) for the high density and small pore width situation. For sufficiently small N_s and sufficiently far from the wall boundary the simulation results are in good agreement with the theory of Sarman and Evans,[25] indicating that the system is in the linear regime. The theory is only valid strictly for homogeneous fluids, so it cannot be expected to hold true near wall boundaries. In the vicinity of the wall, where large gradients exists, we are no longer in the linear regime (see

Downloaded 30 Jun 2008 to 136.186.1.187. Redistribution subject to AIP license or copyright; see http://jcp.aip.org/jcp/copyright.jsp

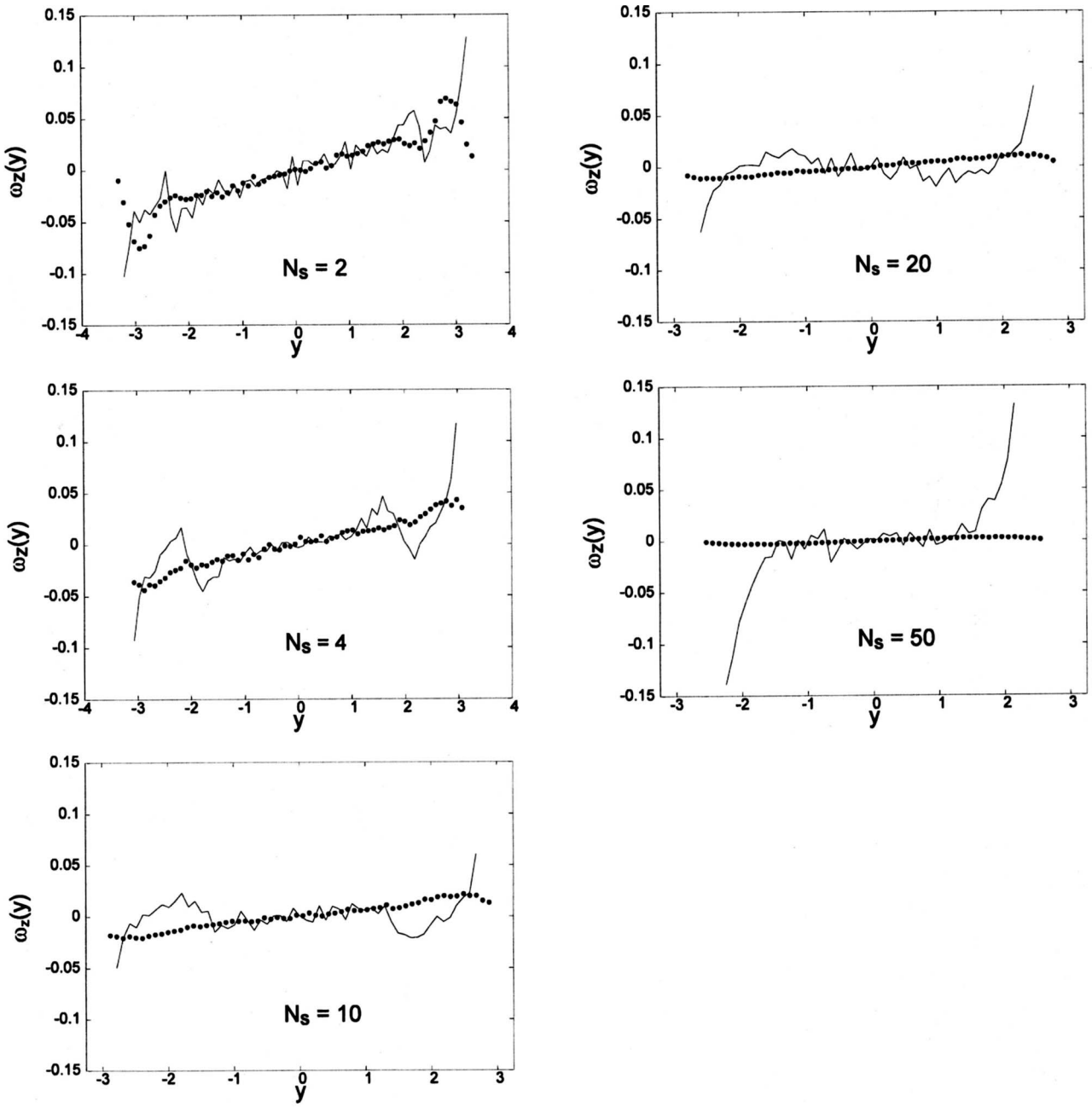

FIG. 19. z components of the streaming angular velocity (filled circles) and one half the vorticity, $1/2\nabla\times\mathbf{u}$ (solid line), for an average fluid density of $\rho=0.65$, external field $F_e=0.05$, and pore width $L=7.0$.

also Fig. 15) and consequently we do not expect the relation $\boldsymbol{\omega}=1/2\nabla\times\mathbf{u}$ to hold. This is also observed in our simulations. Furthermore, as N_s increases the agreement becomes unsatisfactory. The reason for this is that the molecular streaming velocity now shows a weakly quadratic/pluglike flow (as discussed earlier) dramatically affecting the predicted spatial behavior of ω_z leading to an oscillatory profile. The simulation results, however, show that ω_z increases monotonically, at least for systems where $R_g<L$ and $\omega_z\neq 0$. Clearly, when the chain length is such that $R_g>L$, the molecular spin in the x-y plane is severely restricted due to the confinement of molecules in this plane.

IV. CONCLUSIONS

We have studied the rheology of highly confined polymeric fluids undergoing planar Poiseuille flow simulated via nonequilibrium molecular dynamics. The structural and dynamic properties were discussed in terms of the density profiles, the mean squared radius of gyration, the mean squared end-to-end distance, streaming velocity, strain rate, and streaming angular velocity. We examined the scaling behavior of the mean squared radius of gyration and found that, at the pore midpoint, the radius of gyration for chains under shear follows the power law $R_g=AN_b^{\nu}$, where $\nu=0.5$ for both $\rho=0.65$ and 0.45. This is the same as the equilibrium melt value and is an indication that minimal stretching of chains occurred under the shear for the field strengths studied.

We find that the ratio of the square of the end-to-end distance to the square of the radius of gyration is approximately 6 for larger chains sufficiently removed from the walls, a value which is consistent for homogeneous ideal

Downloaded 30 Jun 2008 to 136.186.1.187. Redistribution subject to AIP license or copyright; see http://jcp.aip.org/jcp/copyright.jsp

chain polymeric fluids. We also observe the onset of what appears like plug flow as the molecular length increases relative to the pore width. This effect is not accompanied by significant slip and is more likely to be an effect of restricted molecular layering rather than typical plug-flow behavior. In these cases we find that the strain rates close to the walls are very large compared to the relatively weak strain rates elsewhere.

Finally, we find that the molecular rotation in the interior of the channel, where the system is in the linear regime, can be theoretically predicted through the expression given in Eq. (8), but only for chain lengths sufficiently small compared to the pore width. As N_s increases the prediction becomes less satisfactory, because the molecular rotation is not only dependent on the strain rate but also on the microscopic details of the molecular topology.

ACKNOWLEDGMENTS

The authors thank the Australian Research Council for supporting this work as part of a Discovery Grant. The authors also thank the Australian Partnership for Advanced Computing for a generous allocation of supercomputer time. One of the authors (J.Z.) thanks the Australian Government for financial assistance.

[1] I. Bitsanis, T. K. Vanderlick, M. Tirell, and H. T. Davis, J. Chem. Phys. **89**, 3152 (1988).
[2] H. T. Davis, Chem. Eng. Commun. **58**, 413 (1987).
[3] T. K. Vanderlick and H. T. Davis, J. Chem. Phys. **87**, 1791 (1987).
[4] S. A. Somers and H. T. Davis, J. Chem. Phys. **96**, 5389 (1992).
[5] B. D. Todd, D. J. Evans, and P. J. Daivis, Phys. Rev. E **52**, 1627 (1995).
[6] B. D. Todd and D. J. Evans, Mol. Simul. **17**, 317 (1996).
[7] K. P. Travis, B. D. Todd, and D. J. Evans, Phys. Rev. E **55**, 4288 (1997); K. P. Travis and K. E. Gubbins, J. Chem. Phys. **112**, 1984 (2000).
[8] B. D. Todd and D. J. Evans, Phys. Rev. E **55**, 2800 (1997).
[9] M. Schoen, D. J. Diestler, and J. H. Cushman, J. Chem. Phys. **100**, 7707 (1994); **101**, 6865 (1994).
[10] P. Bordarier, B. Rousseau, and A. H. Fuchs, J. Chem. Phys. **106**, 7295 (1997).
[11] S. T. Cui, P. T. Cummings, and H. D. Cochran, J. Chem. Phys. **111**, 1273 (1999); **114**, 7189 (2001).
[12] S. T. Cui, C. McCabe, P. T. Cummings, and H. D. Cochran, J. Chem. Phys. **118**, 8941 (2003).
[13] F. Varnik, J. Baschnagel, and K. Binder, Eur. Phys. J. E **8**, 175 (2002); F. Varnik, J. Baschnagel, K. Binder, and M. Mareschal, *ibid.* **12**, 167 (2003).
[14] F. Varnik, J. Baschnagel, and K. Binder, Phys. Rev. E **65**, 021507 (2002).
[15] M. Vacatello, Macromol. Theory Simul. **13**, 30 (2004).
[16] J. N. Bright, M. J. Stevens, J. Hoh, and T. B. Woolf, J. Chem. Phys. **115**, 4909 (2001).
[17] A. Sikorski and P. Romiszowski, J. Chem. Phys. **120**, 7206 (2004).
[18] J. Castillo-Tejas, J. F. J. Alvarado, G. González-Alatorre, G. Luna-Bárcenas, I. C. Sanchez, R. Macias-Salinas, and O. Manero, J. Chem. Phys. **123**, 54907 (2006).
[19] K. Kremer and G. S. Grest, J. Chem. Phys. **92**, 5057 (1990).
[20] W. Tschop, K. Kremer, J. Batoulis, T. Burger, and O. Hahn, Acta Polym. **49**, 61 (1998).
[21] W. Tschop, K. Kremer, O. Hahn, J. Batoulis, and T. Burger, Acta Polym. **49**, 75 (1998).
[22] J. D. Weeks, D. Chandler, and H. C. Andersen, J. Chem. Phys. **54**, 5237 (1971).
[23] J. Zhang and B. D. Todd, Phys. Rev. E **69**, 031111 (2004).
[24] K. P. Travis and D. J. Evans, Phys. Rev. E **55**, 1566 (1997).
[25] S. Sarman and D. J. Evans, J. Chem. Phys. **99**, 9021 (1993).
[26] *Monte Carlo and Molecular Dynamics Simulations in Polymer Science*, edited by K. Binder (Oxford University Press, New York, 1995).
[27] T. Matsuda, G. D. Smith, R. G. Winkler, and D. Y. Yoon, Macromolecules **28**, 165 (1995).
[28] I. Bitsanis and G. Ten Brinke, J. Chem. Phys. **99**, 3100 (1993).
[29] M. Doi, *Introduction to Polymer Physics* (Oxford University Press, New York, 1996).
[30] K. F. Freed, *Renormalization Group Theory of Macromolecules* (Wiley, New York, 1987).
[31] P. G. De Gennes, *Scaling Concepts in Polymer Physics* (Cornell University Press, New York, 1979).
[32] T. Kairn, P. J. Daivis, M. L. Matin, and I. K. Snook, Polymer **45**, 2453 (2004).
[33] J. Zhang, B. D. Todd, and K. P. Travis, J. Chem. Phys. **121**, 10778 (2004); **122**, 219901 (2005).
[34] M. Doi and S. F. Edwards, *The Theory of Polymer Dynamics* (Oxford University Press, New York, 1986).
[35] M. Kröger and S. Hess, Phys. Rev. Lett. **85**, 1128 (2000); P. J. Daivis, M. L. Matin, and B. D. Todd, J. Non-Newtonian Fluid Mech. **111**, 1 (2003); J. T. Bosko, B. D. Todd, and R. J. Sadus, J. Chem. Phys. **121**, 12050 (2004).
[36] H. Münstedt, M. Schmidt, and E. Wassner, J. Rheol. **44**, 413 (2000); L. Robert, Y. Demay, and B. Vergnes, Rheol. Acta **43**, 89 (2004).
[37] T. Schmatko, H. Hervet, and L. Leger, Phys. Rev. Lett. **94**, 244501 (2005).
[38] P. J. Cadusch, B. D. Todd, J. Zhang, and P. J. Daivis (unpublished).
[39] B. D. Todd, D. J. Evans, K. P. Travis, and P. J. Daivis, J. Chem. Phys. **111**, 10730 (1999).
[40] R. D. Olmsted and R. F. Snider, J. Chem. Phys. **65**, 3407 (1976).

Downloaded 30 Jun 2008 to 136.186.1.187. Redistribution subject to AIP license or copyright; see http://jcp.aip.org/jcp/copyright.jsp